Structural and Optical Characterization of Reaction Intermediates during Fast Chiral Nanoparticle Growth

Kyle Van Gordon[1,+], Robin Girod[2,+], Francisco Bevilacqua[1], Sara Bals[2], Luis M. Liz-Marzán[1,3,4,5,]*

[1]CIC biomaGUNE, Basque Research and Technology Alliance (BRTA), 20014 Donostia-San Sebastián, Spain

[2]EMAT and NANOLight Center of Excellence, University of Antwerp, B-2020 Antwerp, Belgium

[3]Centro de Investigación Biomédica en Red, Bioingeniería, Biomateriales y Nanomedicina (CIBER-BBN), 20014 Donostia-San Sebastián, Spain

[4]Ikerbasque, 48009 Bilbao, Spain

[5]CINBIO, Universidade de Vigo, 36310 Vigo, Spain

[+]These authors contributed equally

*Corresponding author's email: llizmarzan@cicbiomagune.es

Keywords: chiral nanoparticles, chiral plasmonics, seeded growth, circular dichroism, electron tomography, chiral descriptors, optical-structural relationship

ABSTRACT. As nanoparticle morphologies produced by seeded growth expand in number and complexity, tracking their evolution during growth is increasingly important to achieve mechanistic understanding. However, fast reactions like chiral growth, in which morphologies change within seconds, remain challenging to monitor at the relevant time scale. We introduce a method based on fast addition of the reducing agent $NaBH_4$, enabling interruption of gold nanoparticle growth, as well as access to reaction intermediates for morphological and optical investigations. We show that $NaBH_4$ reduces the remaining gold salt precursors into achiral nanoparticles and prevents further evolution of the target particles, resulting in time series with intervals down to seconds. The method is demonstrated on fast, micelle-directed, chiral growth on

single-crystalline or penta-twinned nanorod seeds, showing fine variations in the temporal evolution of chirality depending on crystal habit. These series provide representative snapshots from a chirality continuum, offering a platform for studying optical-structural relationships.

Colloidal synthesis has become one of the cornerstones of nanoscience.[1] Among a wide variety of systems, metal nanoparticles stand out because of their unique properties leading to applications in various fields.[2,3] Despite many synthetic methods being developed, mechanistic understanding of particle growth is still limited and often based on interpretation of the initial and final timepoints in the synthesis.[4,5] Yet, monitoring the synthetic reaction over time is crucial to analyze the thermodynamic and kinetic aspects of the growth mechanism. In the context of plasmonic particles, access to growth intermediates is essential to correlate morphological evolution and optical response to understand shape-property relationships. Time-resolved experiments have typically involved *in situ* characterization of particle growth: *e.g*. taking measurements during a progressing reaction by spectrophotometry,[6,7] small angle X-ray scattering (SAXS),[8] or electron microscopy.[9] However, both operation and data interpretation for these techniques becomes more demanding when characterizing increasingly complex reactions. For example, seeded-growth reactions involve the reduction of gold salts on pre-made seeds,[10,11] to obtain larger particles or different morphologies. The latter usually requires the presence of additives, such as silver (Ag^+)[12] or iodide[13] ions, to influence anisotropic growth, and a surfactant for colloidal stability which may also influence seeded growth.[14,15] Characterization of the seeded growth of plasmonic nanoparticles by *in situ* optical spectroscopy may be affected by other optically active components that introduce noise in the spectra. Regarding *in situ* electron microscopy, the effects of the electron beam on aqueous solutions are challenging to control and may lead to undesired reduction or sample degradation.[16-18]

An alternative strategy consists of taking aliquots at different timepoints from a progressing synthesis and quenching the chemical reaction by extensive dilution in water or another non-reactive solvent, followed by centrifugation to remove remaining reagents.[19] While this technique may provide interesting information,[20] quenching may not be sufficiently fast to obtain samples that are representative of the selected timepoints. More efficient quenching methods have been proposed, such as the addition of thiolated molecules to passivate both gold nanoparticle surfaces

and unreacted gold salts, thereby enabling structural and optical monitoring of the synthetic reaction at intervals resolved in minutes.[21,22] A common observation when using this method to monitor gold nanorod (Au NR) growth was the formation of a dumbbell-like intermediate before assuming their final prismatic morphology, indicating disproportional growth at particle tips during early growth stages. A similar approach involved the adsorption of various functional groups in cysteine onto growing metal nanomaterials to quench the process.[23] Intermediate structures of Au nanoplates, Pd nanosheets, and Ag nanoprisms (as well as their corresponding optical signatures) could be characterized with a time resolution of seconds. However, high polydispersity was observed at early time points, likely because the progression of the reaction outpaced that of quenching, or because quenching was not complete or uniformly applied to the entire reaction volume.

The recent interest in chiral nanoparticles demands improvements in growth monitoring, given the increased morphological, optical, and synthetic complexity associated with these particles.[24,25] Chiral growth strategies include the use of amino acids as chiral inducers to obtain geometrically twisted particles with smooth surfaces,[26,27] or the introduction of helical micelles (using chiral co-surfactants such as 1,1′-binaphthyl-2,2′-diamine; BINAMINE) to template the growth of helical surface wrinkles on Au NRs.[28] To investigate these complex chiral growth mechanisms, a basic aliquot-and-quench approach has been applied to monitor the growth of chiral Au helicoids at regular time intervals.[29-31] Because the synthesis of helicoids occurs over several hours with a low concentration of reducing agent, an overview of the evolving structure and chiroptical signature could be presented with confidence that the properties would not change significantly during the time required to isolate the particles. However, other chiral growth reactions[26,32,33] use a greater excess of reducing agent and terminate within minutes, therefore requiring a different method to characterize reaction intermediates. In an earlier work, we combined two approaches to monitor micelle-directed chiral growth.[34] A first approach involved *in situ* monitoring by circular dichroism (CD) spectrometry, to record in real time the chiroptical signature of the colloid during chiral growth. Spectroscopic monitoring revealed a critical transition occurring within the first minute of the reaction, indicating that micelle-directed chiral reactions develop even faster than expected. However, this approach was limited by the scan speed and spectral resolution of the CD instrument. In a second approach, optical and morphological characterization was performed by running a

series of growth reactions with varying [$HAuCl_4$]/[Au_{seed}] ratio ($HAuCl_4$ concentration in the growth solution) and recording spectra and electron tomography data sets of the final product. Although interesting morphological information was obtained, it may be argued that the morphologies of particles obtained at low growth solution concentrations may not correspond to those at early stages during the formation of optimized products,[28] obtained with a high [$HAuCl_4$]/[Au_{seed}] ratio.

A method is thus needed to obtain accurate optical and structural information on nanoparticle evolution over timescales ranging from seconds to minutes. We propose a chemical quenching approach to isolate gold nanoparticles at different growth stages, exemplified for micelle-directed chiral growth reactions. We hypothesized that addition of excess sodium borohydride would rapidly terminate a gold nanoparticle growth reaction, thereby allowing the isolation and characterization of products formed at short reaction time intervals.

Addition of excess $NaBH_4$ solution to the reaction medium during chiral overgrowth should exhaust the remaining gold salt precursor by fast reduction into Au^0. The resulting nanoclusters[35,36] could be readily separated from the intermediate chiral products by centrifugation, permitting characterization upon redispersion of the precipitated nanoparticles. By terminating chiral growth at different timepoints and analyzing the products as a series, the chiroptical and structural evolution of a progressing reaction could be assessed. To demonstrate the reliability of this method, the chiroptical spectra of the intermediate products were compared to identical reactions measured *in situ* in a CD spectrometer. By doing so, we ensured that the optical signature of chiral products was not affected by $NaBH_4$, that chiral growth was quickly terminated upon $NaBH_4$ addition, and that the selected timepoints were representative of a reaction in progress.

To ensure fast and complete $HAuCl_4$ reduction while avoiding unwanted reactions, we employed a moderate (1.6×) molar excess of $NaBH_4$, following previous literature.[37] We verified that $NaBH_4$ addition did not affect the growth products, by running identical chiral growth reactions on single-crystalline (SC) nanorod seeds (104.43 ± 5.96 nm x 24.56 ± 1.38 nm) and allowing a sufficient time (30 minutes) for the reaction to be completed.[28] $NaBH_4$ was then added to one of the reactions and the products were isolated by centrifugation and redispersed in water.

Optical spectra from both products were found to be similar (**Figure 1**), with a slight wavelength shift and increased intensity, consistent with surface charging by $NaBH_4$, as previously described for achiral Au NPs[38] and chiral assemblies.[39] We postulate that etching or reshaping of chiral Au NRs would result in a more significant shift and/or reduction in the intensity of the chiroptical signature, and therefore this result indicates no structural damage resulting from $NaBH_4$ addition.

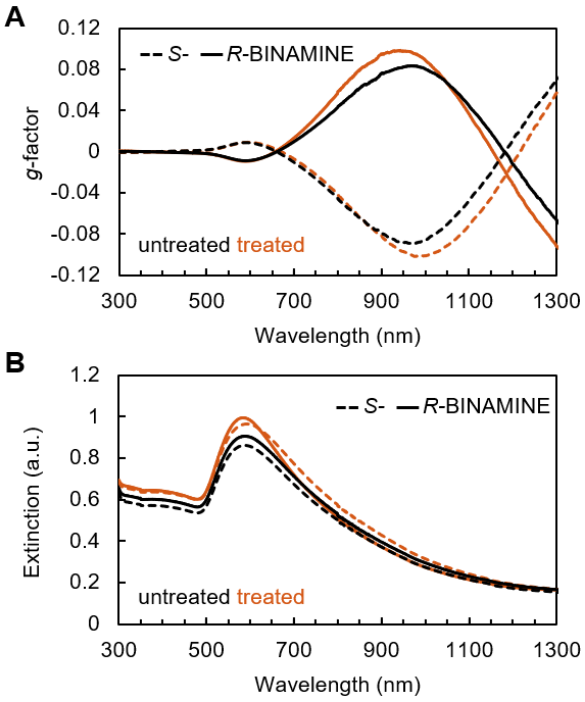

Figure 1. Dissymmetry factor (A) and extinction (B) spectra of untreated (gray lines) *vs.* $NaBH_4$-treated (orange lines) products of micelle-templated chiral growth with *R*- (continuous lines) or *S*-BINAMINE (dashed lines) on achiral SC Au NR seeds. Spectra were recorded after completion of the growth reaction (30 minutes).

We then performed two additional experiments to verify whether seeded growth stops upon $NaBH_4$ addition at the desired timepoint, and the isolated products would be representative of reaction intermediates. We first confirmed that the continuously measured CD signal of a reaction in progress (inside a cuvette) did not change upon $NaBH_4$ addition (**Figure S1**). We also observed the appearance of a brownish color when $NaBH_4$ was added, indicating the formation of nanoclusters. Subsequently, we compared the CD spectra from isolated products with those

continuously recorded *in situ*, at equivalent reaction times (**Figures 2 and S2**). A series of identical reaction mixtures were prepared and $NaBH_4$ was added after 30, 60, 300, or 1800 s. The shade of brown after $NaBH_4$ addition steadily decreased in intensity with increasing reaction time, as expected for the gradual consumption of gold precursor during seeded growth. The product from each timepoint was isolated by centrifugation prior to spectroscopic characterization. The measured chiroptical signatures were compared to those continuously recorded from an identical reaction prepared in a cuvette, inside the CD spectrometer. Results are shown in **Figure 2** for a reaction with *S*-BINAMINE and in **Figure S2** for *R*-BINAMINE. Comparable trends in the spectral features measured at each timepoint are seen, with a systematic 10-40 nm blue-shift and 50-150 mdeg increased magnitude for the CD peaks of *in situ* measured spectra. The magnitude change is likely related to minor product losses during centrifugation, whereas the wavelength shifts can be attributed to the operation of the CD spectrometer in continuous mode. The finite scanning speed and initialization delays cause discrepancies between the time of completion of each scan (reported in Figure 2) and the actual measurement time of the peak CD, which limits the temporal resolution of the instrument (see **Materials and Methods** for details). Nonetheless, these results confirm that the chiroptical signatures of isolated products are consistent with those of untreated products. We propose that the use of $NaBH_4$ offers an advantage over *in situ* measurements by granting access to intermediates at finer time intervals because chiral growth can be quenched at any point after mixing and equilibration. Once redispersed in water, the resulting colloid remains stable and unchanged,[40] enabling the production and characterization of series of products at selected timepoints.

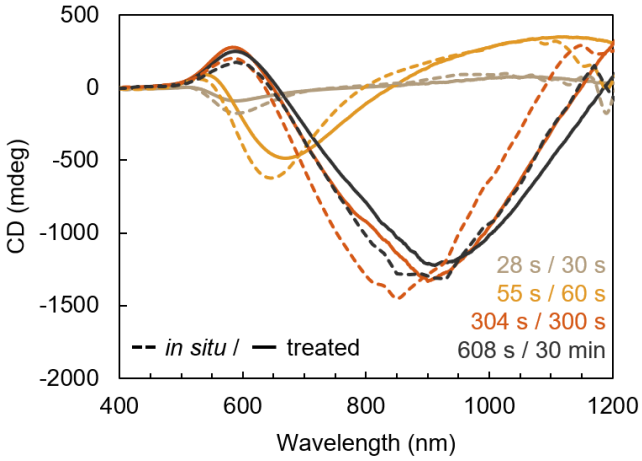

Figure 2. Comparison of chiroptical responses from (solid lines) intermediate products isolated by $NaBH_4$ treatment from chiral growth on SC seeds mediated by *S*-BINAMINE *vs.* (dashed lines) an identically prepared reaction continuously monitored *in situ* in the CD spectrometer (see SI for details). All reactions were prepared at a total volume of 1 mL with 500 μM BINAMINE, 20 mM CTAC, 500 μM $HAuCl_4$, 160 mM ascorbic acid, and 31.25 μM achiral seeds in an Eppendorf tube (for $NaBH_4$ treatment) or a cuvette for optical characterization (for *in situ* monitoring).

We illustrate the merit of such "kinetic series" by investigating the optical and structural transitions during chiral growth mediated by BINAMINE. From the optical characterization in **Figure 2**, it appears that the chiroptical signature reaches its maximum magnitude within the first 2 – 5 minutes of chiral growth. To investigate the morphological factors responsible for this early increase and subsequent decline in CD signal, we replicated our protocol to isolate the products at early (5, 10, 15, 20, 25 s), intermediate (30, 60, 120 s), and late (300, 1800 s) stages of growth, using either *S*-BINAMINE (**Figures 3 and S3**) or *R*-BINAMINE (**Figure S4**). At each timepoint, the morphology of the intermediates was imaged in high-angle annular dark field scanning transmission electron microscopy (HAADF-STEM, **Figure S3A**), characterized in three-dimensions (3D) by electron tomography (ET) in HAADF-STEM mode (**Figure 3A**), and their chiroptical properties were measured by CD spectroscopy (**Figures 3B,C and S3B,C**). This series shows an early intermediate being formed within 5 seconds, featuring 12 facets and a quasi-square cross-section but no chiroptical response. The angles between tip facets and lateral facets are characteristic of fcc crystals enclosed by {110} facets (**Figure S5**). This intermediate is therefore

similar to a previously reported product obtained through reduction of a low [Au^{+}] in BINAMINE-mediated chiral growth.[34] This suggests that the growth pathway does not depend on the concentration of precursors. After this first achiral intermediate, *g*-factors reach values higher than 1% within 25 seconds **(Figure 3B).** This increase in optical activity is in agreement with the noticeable surface texture observed by ET (**Figure 3A**). The emergence of a chiral morphology is further demonstrated by the determination of an increase in total helicity, a shape descriptor determined from the ET data, whose positive values indicate an overall right-handed geometry (**Figure 3D** and **Materials and Methods**).[41] Further increase in optical activity at 60 seconds corresponds to the emergence of distinct wrinkles (**Figure 3A-C**), which become more pronounced and cover the entire particle surface after 120 s (**Figure 3A-C**), coinciding with the time when the *g*-factor approaches a maximum value. Calculations show that this higher *g*-factor correlates with an increase in total helicity, *i.e*. with a stronger predominance of right-handed helical features on the particle surface (**Figure 3D**). At late stages of growth, absorbance increases (**Figure S3C**), whereas CD intensity increases only is stabilized after 300 s. These trends yield a decrease in *g*-factor (CD intensity over absorption) after 300 s (**Figures 3 and S3B**). This could in turn be related to a loss of wrinkle definition, which is not immediately evident from the reconstructions, or to an increase in the proportion of flat wrinkles. Indeed, wrinkled particles present both flat and inclined wrinkles in distinct areas (as seen in **Figure 3A**),[33] and a decreasing total helicity might indicate that areas with flat wrinkles grow faster than those showing inclined wrinkles (see also **Materials and Methods** and **Supplementary discussion** on the behavior of total helicity).

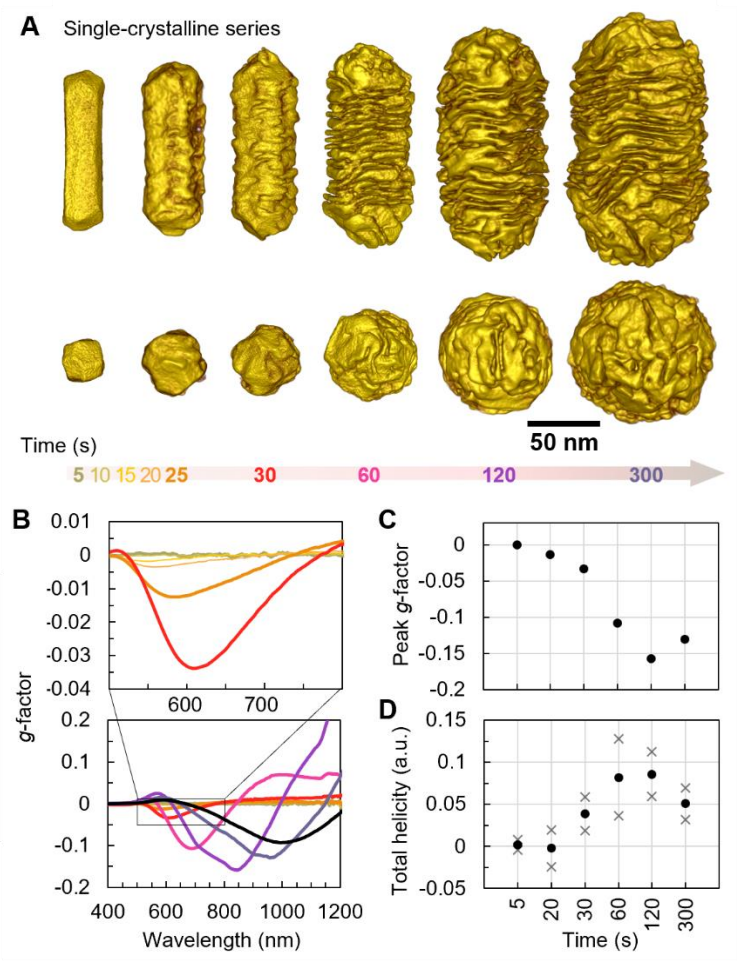

Figure 3. (A) surface renderings of representative electron tomography reconstructions and (B) *g*-factor spectra of nanoparticles isolated from a chiral growth reaction by $NaBH_4$ addition at different time intervals, using SC Au NR seeds and *S*-BINAMINE as the chiral inducer. The upper plot in (B) shows early time points (5 s – 25 s). Spectra are color-coded following the time arrow in (A), the black line corresponds to the end product at 30 min. (C) Dot plot of the peak *g*-factor in the 500-1000 nm range, extracted from the optical spectra. (D) Dot plot of total helicity, extracted from the ET reconstructions, as a function of growth time. Dots are the average of N=2 particles, crosses are the individual values.

We next applied our kinetic series protocol to investigate BINAMINE-induced chiral growth on penta-twinned (PT) Au NRs (82.74 ± 5.86 nm x 20.06 ± 1.45 nm).We have recently reported the unexpected observation that, when starting from PT instead of SC seeds, wrinkled structures are

also obtained albeit with reversed optical and geometrical handedness.[33] To assess whether other differences would be revealed during growth, an identical set of experiments as those in **Figure 3** were carried out, using PT seeds and either *S*- BINAMINE (**Figures 4 and S6**) or *R*-BINAMINE (**Figure S7**), while keeping the proportions of all chemical reagents equivalent, including $NaBH_4$ used to stop the reactions. These syntheses yielded wrinkled particles with dominant left-handed features as seen in ET reconstructions (**Figure 4A**). These qualitative observations are confirmed by calculations showing negative total helicity (**Figure 4C**) and, accordingly, positive *g*-factor (**Figure 4B**). Importantly, the kinetic series shows that growth on PT seeds results in faster optical and morphological transitions than equivalent growth on SC seeds (**Figures 4, S6, and S7**). Surface wrinkling, optical asymmetry and a negative total helicity are already observed after 5 s of growth (**Figure 4**). The chiroptical maximum is reached for particles isolated at 30 s and the ET reconstruction at this timepoint shows particles with well-defined wrinkles (**Figure 4A,C**). After this time, CD intensity, *g*-factor and total helicity decrease (**Figures 4C,D and S6**). Overall, the comparison of the growth series on SC and PT seeds shows that, for chiral growth on SC seeds, a transition stage is required through an achiral intermediate with different geometry and surface facets compared to the starting seed.[34] On the contrary, wrinkle growth on PT seeds can proceed directly on the initial facets. The comparison supports the recently proposed view that wrinkle growth may be guided by geometrical and/or structural factors, rather than micelle handedness alone.[33] These results further support the relevance of a controlled access to the characterization of intermediates, as enabled by our approach.

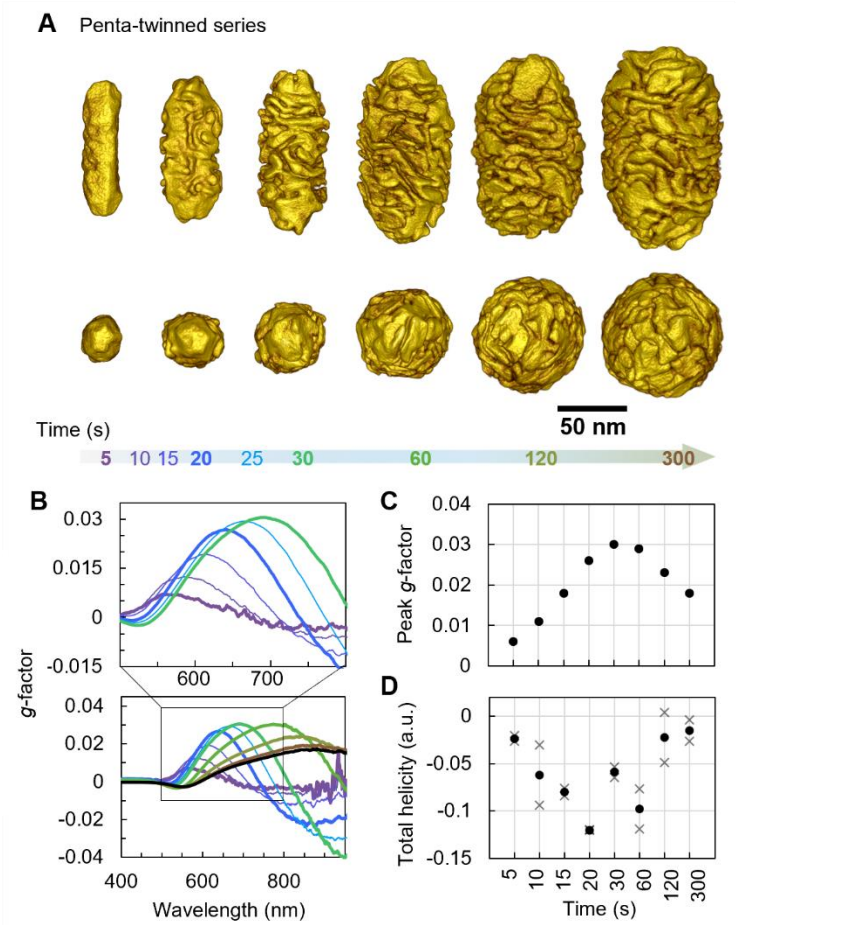

Figure 4. (A) surface renderings of representative electron tomography reconstructions and (B) dissymmetry factor spectra for nanoparticles isolated from a chiral growth reaction by $NaBH_4$ addition at different time intervals, using penta-twinned Au NR seeds and *S*-BINAMINE as the chiral inducer. The upper plot in (B) shows early time intervals (5 s – 25 s). Spectra are color-coded following the time arrow in (A), the black line corresponds to the end product at 30 min. (C) Dot plot of the peak *g*-factor in the 500-1000 nm range, extracted from the optical spectra. (D) Dot plot of total helicity, extracted from the ET reconstructions, as a function of growth time. Dots are the average of N=2 particles, crosses are the individual values. Additional reconstructions at 10 and 15 s are shown in **Figure S8**.

We highlight an additional advantage of the kinetic series by noting that they yield particles with continuously varying optical properties and consistent morphologies. This provides an

excellent platform for the development and statistical test of morphological and chirality descriptors and, in turn, for the study of quantitative structure-properties relationships. This allows us, for instance, to investigate the structural origin of the discrepancy in peak *g*-factor between the two kinetic series: during chiral growth on SC seeds, the g-factor reaches up to 0.12 at 120 s, but peaks at only 0.03 after 30 s of growth on PT seeds (**Figures 3C and 4C**). From the tomography reconstructions, we first extracted morphological measurements of the wrinkles including width, length, and interwrinkle spacing (**Figures 5A,B and S9**), which are known to influence the strength of optical asymmetry.[42] These measurements show that, once complete wrinkle coverage has been achieved (after 60 s on SC seeds, after 30 s on PT seeds), the average wrinkle width and spacing are stable and comparable in both series (on average ~9 nm in width, ~3 nm gaps). The wrinkle length keeps increasing until after 300 s (**Figure 5A,B**), but is thereafter again comparable in both series. Thus, the chiroptical discrepancy in this case likely does not originate from wrinkle dimensions. Chirality descriptors may provide further insights, as we find a clear association between the signs of total helicity and peak *g*-factor (Fisher's exact test, $p = 0.003$), showing that optical handedness could be predicted from the geometrical handedness. Furthermore, these two variables exhibit a remarkably monotonic relationship (**Figure S9A**, Spearman's $\rho = -0.87$, $p = 0.00005$). However, the maximum total helicity is similar in both growth series (~0.1, **Figures 3D and 4D**). Thus, other parameters not captured by total helicity may impact the *g*-factor value. Finally, we investigated wrinkle disorder (**Figure 4D**), which appears to be higher in particles grown from PT seeds than in those grown from SC seeds (as also qualitatively seen in **Figures 3A and 4A**). This structural difference could account for the *g*-factor discrepancy between growth series on SC and PT seeds.

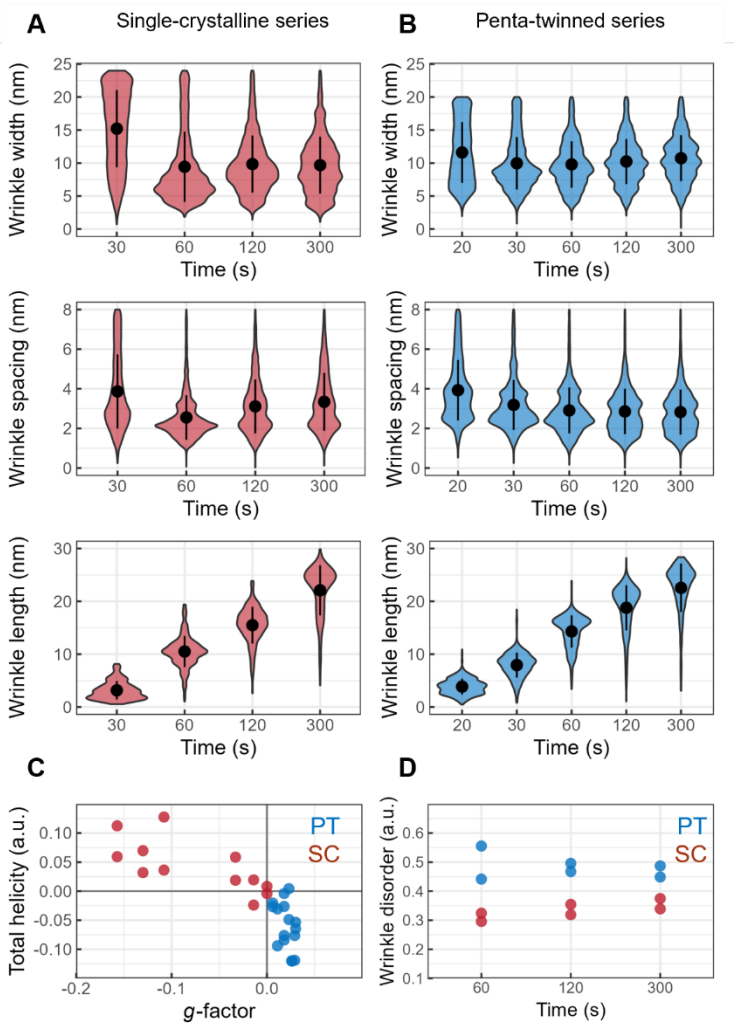

Figure 5. (A, B) Violin plots showing the distribution of (top) wrinkle width, (middle) inter-wrinkle spacing and (bottom) wrinkle length, extracted from electron tomography reconstructions of NPs isolated at various timepoints during chiral growth on (A) SC or (B) PT Au NR seeds with *S*-BINAMINE. At each timepoint, two nanorods, including those shown in **Figures 3 and 4**, were analyzed using an automated volumetric sampling pipeline (see Methods and **Figure S10**). The black dots are the mean and the confidence intervals represent the standard deviation. (C) Total helicity index as a function of the peak *g*-factor for N = 28 wrinkled NRs from the two kinetic series. (D) Wrinkle disorder measured as the variance of surface helical inclination (defined in **Figure S9**) on two nanorods reconstructed for the 60, 120, and 300 s timepoints within the two kinetic series.

In summary, we demonstrated a method to obtain kinetic series by stopping seeded growth reactions through $NaBH_4$ addition and subsequent isolation of intermediate products. The performance of this method was exemplified on micelle-directed chiral growth, starting from both single-crystalline and penta-twinned gold nanorod seeds. Comparison of the absorbance and CD spectra from kinetic series against *in situ* measurements confirmed that products obtained at each timepoint are comparable for both methods. Treatment with $NaBH_4$ was found to suspend a chiral growth reaction, quickly reducing unreacted gold salts without affecting the larger chiral products. This process was signaled by a brownish color arising from the formation of nanoclusters that could be readily isolated from chiral products *via* centrifugation. Intermediate products could be characterized by CD spectroscopy and (3D) electron microscopy techniques, to provide a "snapshot" of the developing optical signature and morphology. This method thus allows monitoring of optical and morphological changes during a nanoparticle growth reaction, providing a platform to investigate optical-structural relationships and to uncover the formation mechanisms of nanoparticles with specific (chiral) properties. Although only presented here for the chiral growth of metal nanoparticles, this method is applicable to a wide variety of nanomaterial compositions, shapes, sizes, as well as the continued design of synthesis methods.

ASSOCIATED CONTENT.

Supporting Information: Experimental details, materials and methods, supplementary discussion on the calculation and behavior of total helicity, additional optical and morphological characterization of chiral gold nanorods (PDF).

Data availability: Raw and processed data, including optical measurements and electron tomography reconstructions, and the code for the calculation of total helicity will be made available on open repositories upon publication.

ACKNOWLEDGEMENTS. The authors acknowledge financial support from MCIN/AEI/10.13039/501100011033 (Grants PID2020-117779RB-I00 and PID2023-151281OB-

I00 to L.M.L.-M, and FPI Fellowship PRE2021-097588 to K.V.G.). R.G. acknowledges the support of a FWO fellowship under award 12A1V25N.

REFERENCES.

1. Liz-Marzán, L. M.; Artzi, N.; Bals, S.; Buriak, J. M.; Chan, W. C. W.; Chen, X.; Hersam, M. C.; Kim, I.-D.; Millstone, J. E.; Mulvaney, P.; Parak, W. J.; Rogach, A.; Schaak, R. E., Celebrating a Nobel Prize to the "Discovery of Quantum Dots, an Essential Milestone in Nanoscience". *ACS Nano* **2023,** *17*, 19474-19475.
2. Montanarella, F.; Kovalenko, M. V., Three Millennia of Nanocrystals. *ACS Nano* **2022,** *16*, 5085-5102.
3. Cho, N. H.; Kim, H.; Kim, J. W.; Lim, Y.-C.; Kim, R. M.; Lee, Y. H.; Nam, K. T., Chiral Inorganic Nanomaterials for Biomedical Applications. *Chem* **2024,** *10*, 1052-1070.
4. Scarabelli, L.; Sánchez-Iglesias, A.; Pérez-Juste, J.; Liz-Marzán, L. M., A "Tips and Tricks" Practical Guide to the Synthesis of Gold Nanorods. *J. Phys. Chem. Lett.* **2015,** *6*, 4270-4279.
5. Wang, S.; Liu, X.; Mourdikoudis, S.; Chen, J.; Fu, W.; Sofer, Z.; Zhang, Y.; Zhang, S.; Zheng, G., Chiral Au Nanorods: Synthesis, Chirality Origin, and Applications. *ACS Nano* **2022,** *16*, 19789-19809.
6. Sharma, V.; Javed, B.; Estrada, G.; Byrne, H. J.; Tian, F., In situ tuning and investigating the growth process of size controllable gold nanoparticles and statistical size prediction analysis. *Coll. Surf. A* **2024,** *681*, 132733.
7. Panariello, L.; Radhakrishnan, A. N. P.; Papakonstantinou, I.; Parkin, I. P.; Gavriilidis, A., Particle Size Evolution during the Synthesis of Gold Nanoparticles Using In Situ Time-Resolved UV–Vis Spectroscopy: An Experimental and Theoretical Study Unravelling the Effect of Adsorbed Gold Precursor Species. *J. Phys. Chem. C* **2020,** *124*, 27662-27672.
8. Polte, J.; Erler, R.; Thunemann, A. F.; Sokolov, S.; Ahner, T. T.; Rademann, K.; Emmerling, F.; Kraehnert, R., Nucleation and growth of gold nanoparticles studied via in situ small angle X-ray scattering at millisecond time resolution. *ACS Nano* **2010,** *4*, 1076-1082.
9. Khelfa, A.; Nelayah, J.; Amara, H.; Wang, G.; Ricolleau, C.; Alloyeau, D., Quantitative In Situ Visualization of Thermal Effects on the Formation of Gold Nanocrystals in Solution. *Adv. Mater.* **2021,** *33*, 2102514.
10. Jana, N. R.; Gearheart, L.; Murphy, C. J., Seeding Growth for Size Control of 5−40 nm Diameter Gold Nanoparticles. *Langmuir* **2001,** *17*, 6782-6786.
11. Jana, N. R.; Gearheart, L.; Murphy, C. J., Seed-Mediated Growth Approach for Shape-Controlled Synthesis of Spheroidal and Rod-like Gold Nanoparticles Using a Surfactant Template. *Adv. Mater.* **2001,** *13*, 1389-1393.
12. Liu, M.; Guyot-Sionnest, P., Mechanism of Silver(I)-Assisted Growth of Gold Nanorods and Bipyramids. *J. Phys. Chem. B* **2005,** *109*, 22192-22200.
13. Sun, Z.; Umar, A.; Zeng, J.; Luo, X.; Song, L.; Zhang, Z.; Chen, Z.; Li, J.; Su, F.; Huang, Y., Highly Pure Gold Nanotriangles with almost 100% Yield for Surface-Enhanced Raman Scattering. *ACS Appl. Nano Mater.* **2022,** *5*, 1220-1231.

14. Zhang, J.; Langille, M. R.; Personick, M. L.; Zhang, K.; Li, S.; Mirkin, C. A., Concave Cubic Gold Nanocrystals with High-Index Facets. *J. Am. Chem. Soc.* **2010,** *132*, 14012-14014.
15. Johnson, C. J.; Dujardin, E.; Davis, S. A.; Murphy, C. J.; Mann, S., Growth and Form of Gold Nanorods Prepared by Seed-Mediated, Surfactant-Directed Synthesis. *J. Mater. Chem.* **2002,** *12*, 1765-1770.
16. Kim, J.; Kang, S.; Cheng, F.; Wang, Y.; Ye, X.; Park, J., Recent Advances in Liquid Phase Transmission Electron Microscopy of Nanoparticle Growth and Self-Assembly. *MRS Bull.* **2024,** *49*, 365-376.
17. Chao, H.-Y.; Venkatraman, K.; Moniri, S.; Jiang, Y.; Tang, X.; Dai, S.; Gao, W.; Miao, J.; Chi, M., *In Situ* and Emerging Transmission Electron Microscopy for Catalysis Research. *Chem. Rev.* **2023,** *123*, 8347-8394.
18. Liao, H.-G.; Niu, K.; Zheng, H., Observation of growth of metal nanoparticles. *Chem. Commun.* **2013,** *49*, 11720-11727.
19. Ji, X.; Song, X.; Li, J.; Bai, Y.; Yang, W.; Peng, X., Size Control of Gold Nanocrystals in Citrate Reduction: The Third Role of Citrate. *J. Am. Chem. Soc.* **2007,** *129*, 13939-13948.
20. Pinho, B.; Zhang, K.; Hoye, R. L.; Torrente-Murciano, L., Importance of Monitoring the Synthesis of Light-Interacting Nanoparticles–A Review on In Situ, Ex Situ, and Online Time-Resolved Studies. *Adv. Optical Mater.* **2022,** *10*, 2200524.
21. Zweifel, D. A.; Wei, A., Sulfide-Arrested Growth of Gold Nanorods. *Chem. Mater.* **2005,** *17*, 4256-4261.
22. Park, K.; Drummy, L. F.; Wadams, R. C.; Koerner, H.; Nepal, D.; Fabris, L.; Vaia, R. A., Growth Mechanism of Gold Nanorods. *Chem. Mater.* **2013,** *25*, 555-563.
23. Ahn, H.; Ahn, H.; Wy, Y.; Han, S. W., Suppressing Nanocrystal Growth with Cysteine: A Quenching Strategy for Monitoring the Evolution of Nanocrystals. *Chem. Mater.* **2023,** *35*, 10533-10541.
24. Cho, N. H.; Guerrero-Martínez, A.; Ma, J.; Bals, S.; Kotov, N. A.; Liz-Marzán, L. M.; Nam, K. T., Bioinspired Chiral Inorganic Nanomaterials. *Nat. Rev. Bioengineering* **2023,** *1*, 88-106.
25. Ni, B.; González-Rubio, G.; Van Gordon, K.; Bals, S.; Kotov, N. A.; Liz-Marzán, L. M., Seed-Mediated Growth and Advanced Characterization of Chiral Gold Nanorods. *Adv. Mater.* **2024,** *36*, 2412473.
26. Ni, B.; Mychinko, M.; Gómez-Graña, S.; Morales-Vidal, J.; Obelleiro-Liz, M.; Heyvaert, W.; Vila-Liarte, D.; Zhuo, X.; Albrecht, W.; Zheng, G.; González-Rubio, G.; Taboada, J. M.; Obelleiro, F.; López, N.; Pérez-Juste, J.; Pastoriza-Santos, I.; Cölfen, H.; Bals, S.; Liz-Marzán, L. M., Chiral Seeded Growth of Gold Nanorods Into Fourfold Twisted Nanoparticles with Plasmonic Optical Activity. *Adv. Mater.* **2023,** *35*, 2208299.
27. Lee, H.-E.; Ahn, H.-Y.; Mun, J.; Lee, Y. Y.; Kim, M.; Cho, N. H.; Chang, K.; Kim, W. S.; Rho, J.; Nam, K. T., Amino-Acid and Peptide-Directed Synthesis of Chiral Plasmonic Gold Nanoparticles. *Nature* **2018,** *556*, 360-365.
28. González-Rubio, G.; Mosquera, J.; Kumar, V.; Pedrazo-Tardajos, A.; Llombart, P.; Solís, D. M.; Lobato, I.; Noya, E. G.; Guerrero-Martínez, A.; Taboada, J. M.; Obelleiro, F.; MacDowell, L. G.; Bals, S.; Liz-Marzán, L. M., Micelle-Directed Chiral Seeded Growth on Anisotropic Gold Nanocrystals. *Science* **2020,** *368*, 1472-1477.

29. Cho, N. H.; Byun, G. H.; Lim, Y.-C.; Im, S. W.; Kim, H.; Lee, H.-E.; Ahn, H.-Y.; Nam, K. T., Uniform Chiral Gap Synthesis for High Dissymmetry Factor in Single Plasmonic Gold Nanoparticle. *ACS Nano* **2020,** *14*, 3595-3602.
30. Cho, N. H.; Kim, Y. B.; Lee, Y. Y.; Im, S. W.; Kim, R. M.; Kim, J. W.; Namgung, S. D.; Lee, H.-E.; Kim, H.; Han, J. H.; Chung, H. W.; Lee, Y. H.; Han, J. W.; Nam, K. T., Adenine Oligomer Directed Synthesis of Chiral Gold Nanoparticles. *Nat. Commun.* **2022,** *13*, 3831.
31. Im, S. W.; Jo, E.; Kim, R. M.; Han, J. H.; Nam, K. T., 32-Symmetric Chiral Gold Nanoplates with Near-Infrared Circular Dichroism. *Adv. Optical Mater.* **2023,** *11*, 2300037.
32. Van Gordon, K.; Baúlde, S.; Mychinko, M.; Heyvaert, W.; Obelleiro-Liz, M.; Criado, A.; Bals, S.; Liz-Marzán, L. M.; Mosquera, J., Tuning the Growth of Chiral Gold Nanoparticles Through Rational Design of a Chiral Molecular Inducer. *Nano Lett.* **2023,** *23*, 9880-9886.
33. Van Gordon, K.; Ni, B.; Girod, R.; Mychinko, M.; Bevilacqua, F.; Bals, S.; Liz-Marzán, L. M., Single Crystal and Pentatwinned Gold Nanorods Result in Chiral Nanocrystals with Reverse Handedness. *Angew. Chem. Int. Ed.* **2024,** *63*, e202403116.
34. Zhuo, X.; Mychinko, M.; Heyvaert, W.; Larios, D.; Obelleiro-Liz, M.; Taboada, J. M.; Bals, S.; Liz-Marzán, L. M., Morphological and Optical Transitions during Micelle-Seeded Chiral Growth on Gold Nanorods. *ACS Nano* **2022,** *16*, 19281-19292.
35. Brust, M.; Walker, M.; Bethell, D.; Schiffrin, D. J.; Whyman, R., Synthesis of Thiol-derivatised Gold Nanoparticles in a Two-phase Liquid–Liquid system. *Chem. Commun.* **1994**, 801-802.
36. Brust, M.; Fink, J.; Bethell, D.; Schiffrin, D.; Kiely, C., Synthesis and Reactions of Functionalised Gold Nanoparticles. *Chem. Commun.* **1995**, 1655-1656.
37. Gonzalez-Rubio, G.; Kumar, V.; Llombart, P.; Diaz-Nunez, P.; Bladt, E.; Altantzis, T.; Bals, S.; Pena-Rodriguez, O.; Noya, E. G.; MacDowell, L. G.; Guerrero-Martinez, A.; Liz-Marzan, L. M., Disconnecting Symmetry Breaking from Seeded Growth for the Reproducible Synthesis of High Quality Gold Nanorods. *ACS Nano* **2019,** *13*, 4424-4435.
38. Mulvaney, P.; Pérez-Juste, J.; Giersig, M.; Liz-Marzán, L. M.; Pecharromán, C., Drastic Surface Plasmon Mode Shifts in Gold Nanorods Due to Electron Charging. *Plasmonics* **2006,** *1*, 61-66.
39. Kumar, J.; López-Martínez, E.; Cortajarena, A. L.; Solís, D. M.; Taboada, J. M.; Díez-Buitrago, B.; Pavlov, V.; Liz-Marzán, L. M., Charge-Induced Shifts in Chiral Surface Plasmon Modes in Gold Nanorod Assemblies. *Part. Part. Syst. Charact.* **2019,** *36*, 1800368.
40. Zhuo, X.; Vila-Liarte, D.; Wang, S.; Jimenez de Aberasturi, D.; Liz-Marzán, L. M., Coated Chiral Plasmonic Nanorods with Enhanced Structural Stability. *Chem. Mater.* **2023,** *35*, 5689-5698.
41. Heyvaert, W.; Pedrazo-Tardajos, A.; Kadu, A.; Claes, N.; González-Rubio, G.; Liz-Marzán, L. M.; Albrecht, W.; Bals, S., Quantification of the Helical Morphology of Chiral Gold Nanorods. *ACS Materials Lett.* **2022,** *4*, 642-649.
42. Obelleiro-Liz, M.; Martín, V. F.; Solís, D. M.; Taboada, J. M.; Obelleiro, F.; Liz-Marzán, L. M., Influence of Geometrical Parameters on the Optical Activity of Chiral Gold Nanorods. *Adv. Optical Mater.* **2023,** *11*, 2203090.

TABLE OF CONTENTS GRAPHIC

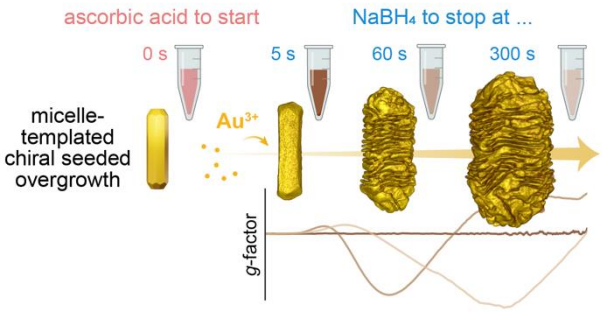

Supplementary information

Structural and Optical Characterization of Reaction Intermediates during Fast Chiral Nanoparticle Growth

Kyle Van Gordon[1,+], Robin Girod[2,+], Francisco Bevilacqua[1], Sara Bals[2], Luis M. Liz-Marzán[1,3,4,5,]*

[1]CIC biomaGUNE, Basque Research and Technology Alliance (BRTA), 20014 Donostia-San Sebastián, Spain

[2]EMAT and NANOLight Center of Excellence, University of Antwerp, B-2020 Antwerp, Belgium

[3]Centro de Investigación Biomédica en Red, Bioingeniería, Biomateriales y Nanomedicina (CIBER-BBN), 20014 Donostia-San Sebastián, Spain

[4]Ikerbasque, 48009 Bilbao, Spain

[5]CINBIO, Universidade de Vigo, 36310 Vigo, Spain

[+]These authors contributed equally

*Corresponding author's email: llizmarzan@cicbiomagune.es

Materials and Methods

Materials

$HAuCl_4 \cdot 3H_2O$ (99.99% (metals basis)) was purchased from Alfa Aesar. Ascorbic acid (AA) was purchased from Acros Organics. $AgNO_3$ (>99.9%) was purchased from Roth. (*R*)-(+)-1,1′-binaphthyl-2,2′-diamine (*R*-BINAMINE, 99%), (*S*)-(−)-1,1′-binaphthyl2,2′-diamine (*S*-BINAMINE, 99%), cetyltrimetryammonium chloride (CTAC, >98.0%), cetyltrimethylammonium bromide (CTAB; 99%), n-decanol (for synthesis; ≥ 99.0%), sodium borohydride ($NaBH_4$; 99%), and ascorbic acid (AA; ≥ 99%) were all purchased from Sigma-Aldrich. Hydrochloric acid (HCl; ACS, ISO grade, 3% w/v) was sourced from Scharlau. All reagents were used as received without further purification. MilliQ water was used to prepare solutions.

Preparation of single-crystalline gold nanorods (SC-Au NRs) for chiral syntheses

Single-crystalline achiral Au NRs were synthesized according to a protocol adapted from the literature.[1,2] To an 80 mL solution of 50 mM CTAB and 11 mM *n*-decanol prepared in a glass vial, 9.6 mL HCl solution (aq., 1 M), 1.2 mL $AgNO_3$ solution (aq., 50 mM), and 800 µL $HAuCl_4$ solution (aq., 50 mM) were added sequentially under constant magnetic stirring. After thorough sonication, 640 µL ascorbic acid solution (aq., 100 mM) was added under constant magnetic stirring until the solution became colorless. Gold mini-rod seeds (ca. 21 x 7.5 nm) prepared and concentrated according to established literature,[1] were then added to the mixture (7 µL, $[Au^0]$ = 29.8 mM). After overnight incubation at 16 °C in a temperature-controlled water bath, the solution turned a reddish-brown color. Synthesized nanorods were purified by three rounds of centrifugation (4250 *g*, 30 min); after each round, the supernatant was discarded, and the particles redispersed in 1 mM CTAC. To assist removal of CTAB and Ag^+ ions, nanorod dispersions were heated at 60 °C for 30 min before each round of centrifugation.

Preparation of penta-twinned gold nanorods (PT-Au NRs) for chiral syntheses

Achiral pentatwinned Au NRs were synthesized according to a protocol adapted from the literature.[3,4] Pentatwinned Au seeds were first prepared by adding a 0.05 M $HAuCl_4$ solution (50 µL) to 10 mL of 50 mM CTAC and 5 mM citric acid. After 30 minutes, a solution of a 25 mM $NaBH_4$ solution (250 µL) was rapidly added to the mixture, for reasons similar to those detailed in

the synthesis of single-crystalline seeds. After a further 2 minutes, the seeds were aged for 90 min at 80 ºC with stirring to induce twinning. Formation of pentatwinned seeds is indicated by the appearance of a strong LSPR peak in the linear optical spectrum around 550 nm.

For nanorod growth, a 0.05 M $HAuCl_4$ solution (125 µL) was mixed with 50 mL of 8 mM CTAB. The mixture was stored at 20 °C for at least 15 minutes, to allow for complete complexation between Au^{3+} and CTAB. After this time, a 0.1 M solution of AA (125 µL) was added, followed by 100 µL of pentatwinned Au seed dispersion ($[Au^{3+}] : [Au^0] = 1.25$). The reaction mixture was left undisturbed overnight, and then centrifuged at 4250 *g* for 10 min and washed with 10 mM CTAC thrice.

Seeded chiral growth in the presence of BINAMINE

Chiral products were synthesized in the presence of BINAMINE according to established literature.[5-8] For chiral particles prepared using BINAMINE, seeds were first incubated overnight in a solution of 50 mM CTAC and 1.25 mM *R*- or *S*- BINAMINE. A typical chiral synthesis was prepared in an Eppendorf tube at a total volume of 1 mL, using 500 µM BINAMINE, 20 mM CTAC, 500 µM $HAuCl_4$, 160 mM ascorbic acid, and 31.25 µM achiral seeds. Seeds and ascorbic acid were sequentially added, and the tube was immediately shaken and then left for 30 minutes at room temperature. Chiral particles were centrifuged at 4250 *g* for 10 minutes and resuspended in MilliQ-grade water. This process was repeated twice to separate chiral products from excess reagents and non-chiral reaction byproducts.

Kinetic series for chiral nanoparticle synthesis

To stop a chiral reaction in progress via the rapid reduction of gold salts ($HAuCl_4$) contributing to overgrowth, 1.6 molar equivalents of $NaBH_4$ was added, as compared to the amount of gold salt present in the reaction, as dictated by literature reports.[1] For a 1 mL chiral reaction volume with $[HAuCl_4]$ = 500 µM, an ice-cold solution of 20 mM $NaBH_4$ is prepared, and 40 µL of this solution transferred to the chiral reaction in progress. The reaction tube is then shaken to rapidly reduce the gold salts; this is indicated by the fast appearance of a brown color in solution. Time zero of the reaction is represented by when ascorbic acid is added to initiate chiral overgrowth; a given time point in a kinetic series is represented by the time elapsed before $NaBH_4$ addition. Chiral particles are isolated via centrifugation at 4250 *g* for 10 minutes and resuspended in MilliQ-grade

water. This process was repeated twice to separate chiral products from excess reagents and non-chiral reaction byproducts.

Optical characterization

All circular dichroism (CD) spectra were acquired using a JASCO J-1500 CD spectrometer in CD/DC mode, measuring the differential absorption of circularly polarized light by the sample as a function of the direct current (DC) measured by the detector.

For samples measured continuously, seeded chiral growth reactions were prepared identically to the above description, but in a quartz cuvette. The CD instrument was set to capture a wavelength range between 390 and 1250 nm, at a spectral resolution (data pitch) of 20 nm and a scan rate of 5000 nm/min. Time zero is represented by the first scan of the CD instrument, which was initialized immediately after the addition of ascorbic acid to the reaction. A reinitialization time is required during scans, bringing the actual time between the starts of two consecutive scans to 25-30 s. This duration had some variability and the acquired CD spectra are therefore reported herein by their collection time by the instrument, i.e., the time at which the scan was completed.

For all other samples, CD spectra were acquired in two steps, from 300 nm to 900 nm (using a PMT detector) and from 800 nm to 1300 nm (using an InGaAs detector). Both spectra were then combined using "spectra concatenation" software from JASCO to obtain a CD spectrum from 300-1300 nm. The concatenation provides higher resolution but may occasionally introduce an artifactual "bump" in range 800-900 nm that did not influence the analyses herein.

A Cary 50 UV Visible spectrophotometer from Agilent Technologies was used to collect UV-Vis optical spectra.

Characterization by electron microscopy and electron tomography

Overview images were acquired soon after synthesis at a JEOL 2200FS transmission electron microscopy (TEM) operated at 200 kV in high angle annular-dark-field (HAADF) scanning TEM (STEM) mode.

Acquisition of tilt-series for electron tomography was performed at a ThermoFisher Scientific Osiris or a Titan cubed operated at 200 kV or 300 kV, respectively. Imaging was performed in

HAADF-STEM mode with a 50-60 pA probe current, 15-17 mrad convergence angle, and 46-215 mrad collection angle at the HAADF detector equivalent to a 115 mm camera length on our microscopes. Tilt-series were acquired using a Fischione 2020 single-axis tomography holder, typically in a [-75, +75]° range. Acquisition was either manual with 3° angular increments, or using an software developed in-house for fast acquisition with incremental tilts of 2° angular steps.[9] The tilt-series were aligned with cross-correlation using an in-house developed Matlab code and 3D reconstructions were computed with the standard expected maximization (EM) algorithm using the Astra toolbox 2.1 for Matlab.[10,11] Isosurface renderings were created with Amira (v5.4.0). At least two particles were reconstructed for each sample analyzed.

Helicity analysis from electron tomography reconstructions

Helicity analysis was conducted following methods we presented in previous work.[6,12] Briefly, the total helicity of a closed surface is defined following:

$$H_{total} := \frac{\oiint_S \mathrm{sign}(\alpha) dS}{\oiint_S dS} \tag{1}$$

Where S is the surface of the particle under investigation and α is the helical inclination angle of an infinitesimal surface element. This angle is defined by analogy with the inclination angle mathematically defining a helix and can be calculated for each surface element of a *cylindrical* triangulated mesh following:

$$\alpha = \left[\left(\arctan\left(\frac{n_z}{n_\theta}\right) + \pi\right) \mod \pi\right] - \frac{\pi}{2} \tag{2}$$

Where n_z is the axial component and n_θ is the azimuthal component of the normal vector **N** expressed in cylindrical coordinates of the surface element, as schematically depicted in **Figure S10**. Thus, for a mesh of *i* elements:

$$H_{total} := \frac{\sum_i \mathrm{sign}(\alpha_i) S_i}{\sum_i S_i} \tag{3}$$

Where α_i and S_i are the helical inclination angle and surface area of element *i*, respectively. By definition, α will be positive for a surface element inclined at a right-handed angle, resp. negative for a left-handed angle. It follows from equation 3 that:

$$H_{total} := \frac{S_{\alpha>0}}{S} - \frac{S_{\alpha<0}}{S} \quad (4)$$

Which reads: the total helicity is the difference between the fraction a particle's surface area that is right-handed (inclined positively) and the fraction that is left-handed (inclined negatively). If there is an excess of right-handed surface features, the total helicity will be positive resp. negative if there is an excess of left-handed surface features. If there is an equal amount of right-handed and left-handed surface, i.e., a non-helical geometry, the total helicity will be null.

For the analysis, each electron tomography reconstruction was binarized with a manual threshold and its surface mesh was extracted by triangulation using the built-in Amira module. The mesh was rotated to have the long axis of the nanorod aligned in the **z** direction and the helical inclination angle was calculated for each surface elements. To focus on the central part of the rods which is the section that best fulfills the geometrical assumptions underlying the calculation of the helical inclination angle, the top and bottom 15% of the rods were removed. For each particle, the total helicity was calculated as detailed above and a helicity plot was generated, showing the distribution of surface inclinations as a function of the radial position of the surface elements (**Figure S11**). The statistical tests on the association between total helicity and the magnitude of the peak g-factor were done with R (v.4.3.2.). For helicity, the average value of N=2 particles per sample was used.

Disorder analysis from electron tomography reconstructions

For disorder analysis, the variance of the distribution of helical inclination angle α (see above) on a particle was used as a proxy measurement. In effect, a high variance indicates a wide distribution of inclination angles, regardless of the excess of right-handed to left-handed inclinations (and thus of helicity). Conversely, a low variance indicates a narrower distribution of inclination angles and that the wrinkles are more ordered. The analysis was conducted on time points in which distinct wrinkles had already developed, i.e., 60, 120, and 300 s for both growth series on SC and PT seeds.

Morphological analyses of wrinkles from electron tomography reconstructions

For each electron tomography reconstructions with distinct wrinkles (i.e., after 30 s of growth in the growth series on SC seeds, 20 s of growth in the series on PT seeds), a distribution of wrinkle width, length and interwrinkle spacing was measured using an automated python workflow schematically described in **Figure S12**. In detail, the background was first removed using a triangle

threshold,[14] and the result was binarized at Otsu's threshold[15], both calculated using the sci-kit image python implementation. The background removal was paramount to ensure that Otsu's threshold provided comparable delineation of the wrinkles across all reconstructions. Then, the 3D local thickness at each voxel within the particle phase was computed using the `fast local thickness` python toolbox.[16] The local thickness is defined as the diameter of the largest inscribed sphere that contains the specific voxel for which it is computed. The local thickness is computed for each voxel of the volume of interest and thus yields a thickness map, whose histogram (whether fully or partially sampled) shows the distribution of thickness (see **Figure S12C**). Here, all voxels with a local thickness larger than the diameter of the seed (~ 24 nm for SC Au NR seeds, ~ 20 nm for PT Au NR seeds) were assumed to belong to the core. Conversely, all voxels with a local thickness below these cutoffs were assumed to belong to the wrinkle corona. **Figure S12D** shows that this assumption is indeed valid. After applying the cutoff, the remaining voxels effectively form a map of the wrinkle width. To plot the distributions, N = 10,000 non-zero points per reconstruction were randomly sampled within these maps.

To measure the interwrinkle spacing, a similar workflow was followed but the local thickness map was computed on the background phase obtained after Otsu's threshold (**Figure S12E)**. For all Au NRs, a cutoff at 8 nm was used, assuming that all voxels with a local thickness below this value belong the wrinkle interspace. **Figure S12F** again shows that this assumption is correct. For the distributions, N = 10,000 non-zero points per particle were randomly sampled in the maps.

Finally, the wrinkle length distribution was obtained by first computing a binary volume of all non-zero voxels in the wrinkle width and interwrinkle spacing maps, thus isolating the {wrinkle + interwrinkle space} corona under the previous assumptions (**Figure S12G**), before computing the local thickness again. This is done so that the diameter of the largest inscribed sphere (the local thickness) is set by the width of the corona, i.e., so that a map of the wrinkle length is obtained. This effectively assumes that wrinkles are straight, which is an assumption better fulfilled for the wrinkles growing on SC seeds than those grown on PT seeds.[13] Therefore, this method slightly underestimates the length of wrinkles growing on the latter. For the distributions, N = 1,000 non-zero points were randomly sampled in the maps.

Supplementary Discussion: helicity and dimensions of wrinkles

Here we provide insights into how the total helicity would change with the wrinkles' dimensions. First, we need to establish that the surface elements *i* of a particle as present in eq. 3 can be classified in three categories:

- Surface elements *j* belong to locally *non-inclined* areas. This would for instance be an area without wrinkles or one with flat wrinkles.[13] Importantly, because of the way α is defined (eq. 2), this is also the case of the *edge* of a wrinkle (**Figure S10**). Here, $\sum_j \mathrm{sign}(\alpha_j) S_j = 0$, recalling that S_j is the surface area of element *j*.
- Surface elements *k* belong to *inclined* features whose handedness is matched *at the particle level* by other features of opposite handedness. In other words, elements *k* are inclined but not in excess of one handedness, so that, here again, $\sum_k \mathrm{sign}(\alpha_k) S_k = 0$. For wrinkled particles, this could for instance be related to the presence of both right-handed and left-handed wrinkles around the particles.[6]
- Surface elements *l* belong to the remaining features (in set notation, $\{l\} = \{i\} - (\{k\} \cup \{j\})$) that are *inclined* and in strict *excess* of one handedness. It follows that $\sum_l \mathrm{sign}(\alpha_l) S_l = \pm S_L$. We stress that, following the point made for the elements *j*, only the *upper* and *lower* sides of a wrinkle (**Figure S10**) can host *l* elements and therefore contribute to S_L.

With these definitions, eq. 3 simplifies to:

$$H_{total} := \frac{\pm S_L}{S} \tag{4}$$

Because only the upper and lower sides of the wrinkles contribute to S_L, it becomes apparent that the wrinkles' dimensions will affect the total helicity. For instance, longer wrinkles or a shorter inter-spacing increase the fraction of surface elements that are part of these upper or lower areas of the wrinkles. This means, all inclinations being constant, an increase in the fraction of excess inclined elements S_L/S and, in turn, H_{total}.

Supplementary Figures S1-S12

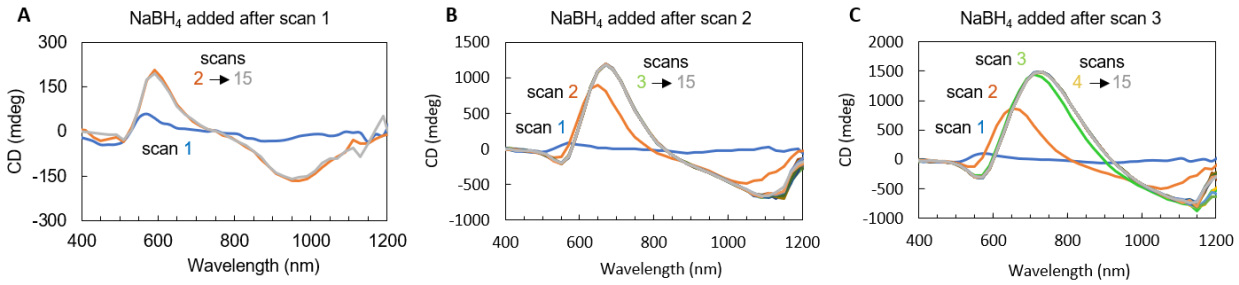

Figure S1. Effect of $NaBH_4$ addition on the chiroptical response from *R*-BINAMINE-induced chiral growth reactions using single-crystalline Au NR seeds. Three reactions were measured *in situ* and treated with $NaBH_4$ after 1 scan (A), 2 scans (B), or 3 scans (C). 15 scans in the 390-1250 nm range were recorded continuously. The scan rate was 5000 nm/min, with an additional reinitialization delay bringing the time between two scans to ~28 s on average. The spectra do not vary past the scan where $NaBH_4$ was added and we conclude that $NaBH_4$ addition therefore stops the reaction faster than the spectrometer can measure it. The presence of a weak CD signal during the first scan is explained by the limited scan speed and an initialization delay.

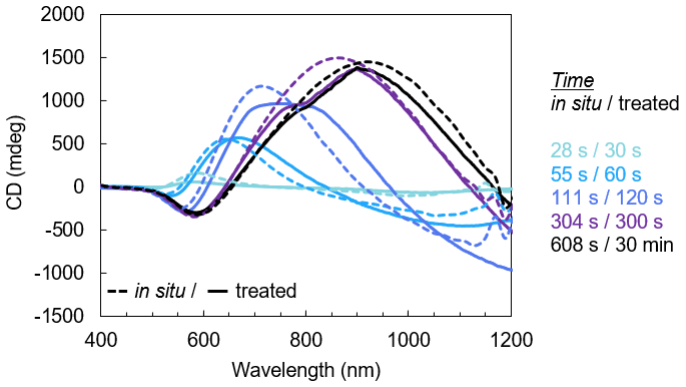

Figure S2. Comparison of the chiroptical response from *R*-BINAMINE micelle-templated intermediates isolated by $NaBH_4$ treatment (solid lines) *vs.* continuously monitored *in situ* (dashed lines). Single-crystalline Au NRs were used as seeds.

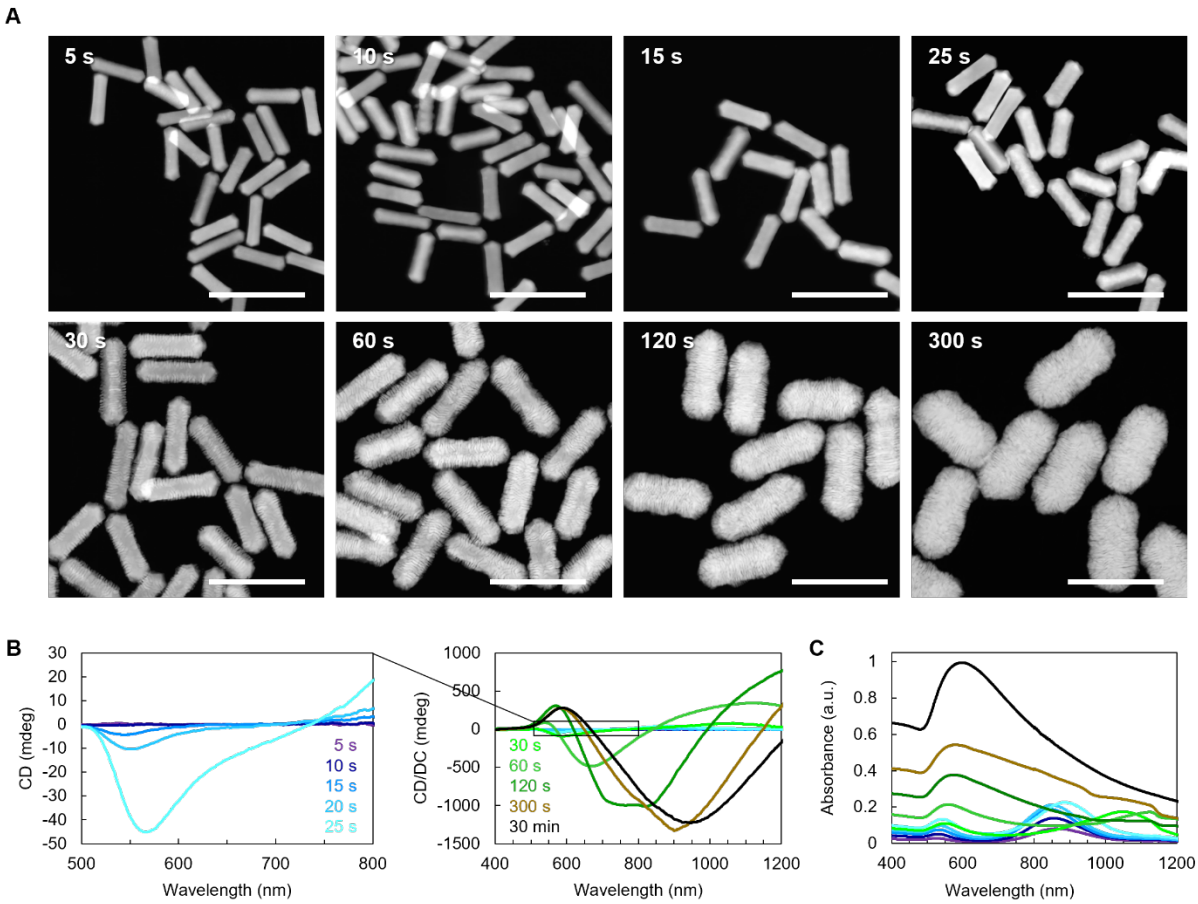

Figure S3. Additional characterization for the kinetic series shown in **Figure 3** of the main text. Nanoparticles isolated from a chiral growth reaction by $NaBH_4$ addition at different time intervals, using SC Au NR seeds and *S*-BINAMINE as the chiral inducer. (A) HAADF-STEM imaging, (B) CD and (C) Absorbance measurements. The scale bars are 200 nm.

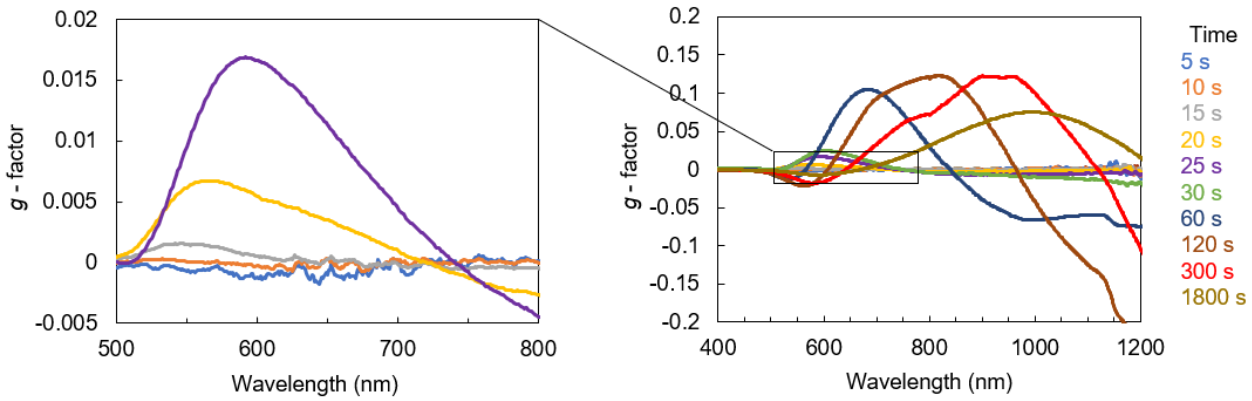

Figure S4. Chiroptical factor spectra of nanoparticles isolated from a chiral growth reaction by $NaBH_4$ addition at different time intervals, using single-crystalline Au NR seeds and *R*-BINAMINE as the chiral inducer.

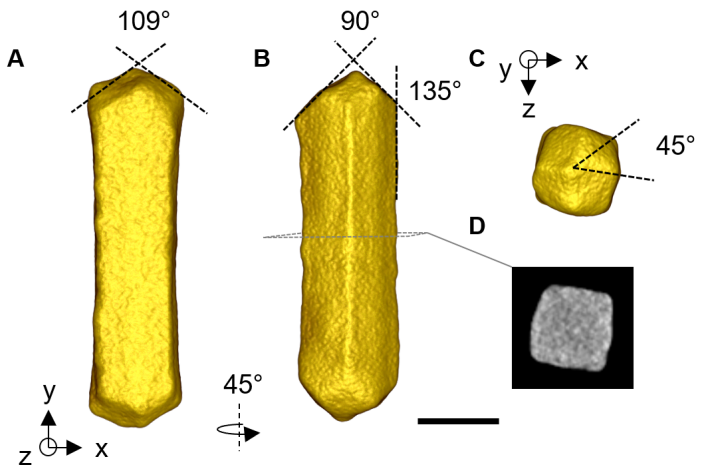

Figure S5. Details of the electron tomography reconstruction in **Figure 3A** presenting a particle isolated at 5 s of chiral growth using single-crystalline Au NR seeds and *S*-BINAMINE. (A-C) isosurface rendering and (D) orthoslice through the reconstruction. The particle features 12 faces: 4 lateral ones and 8 at the tips. The angles are consistent with an fcc crystal enclosed by 12 {110} facets. The orthoslice shows a quasi-square cross section and that the lateral faces are less concave than previously reported.[7] The scale bar is 25 nm.

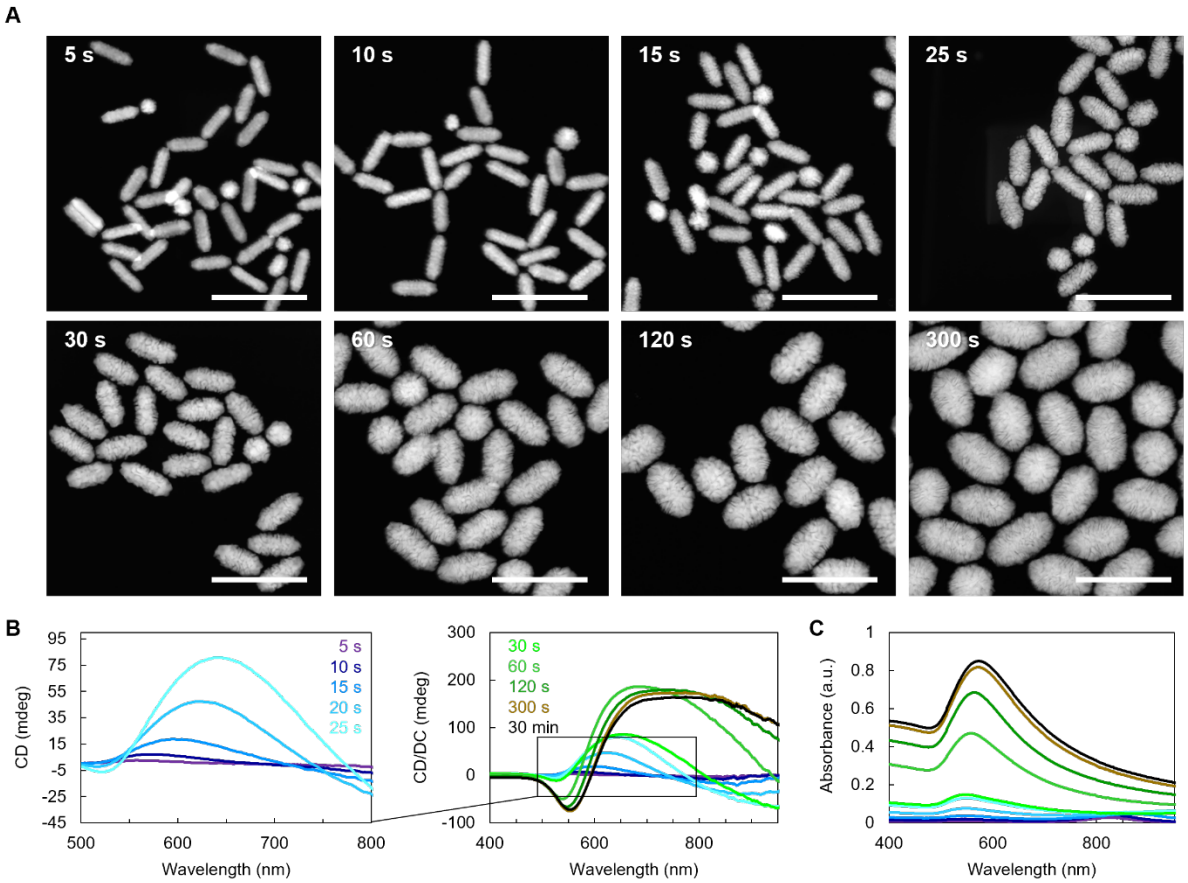

Figure S6. Additional characterization for the kinetic series shown in **Figure 4** of the main text. Nanoparticles were isolated from a chiral growth reaction by $NaBH_4$ addition at different time intervals, using penta-twinned Au NR seeds and *S*-BINAMINE as the chiral inducer. (A) HAADF-STEM imaging, (B) CD and (C) Absorbance measurements. The scale bars are 200 nm.

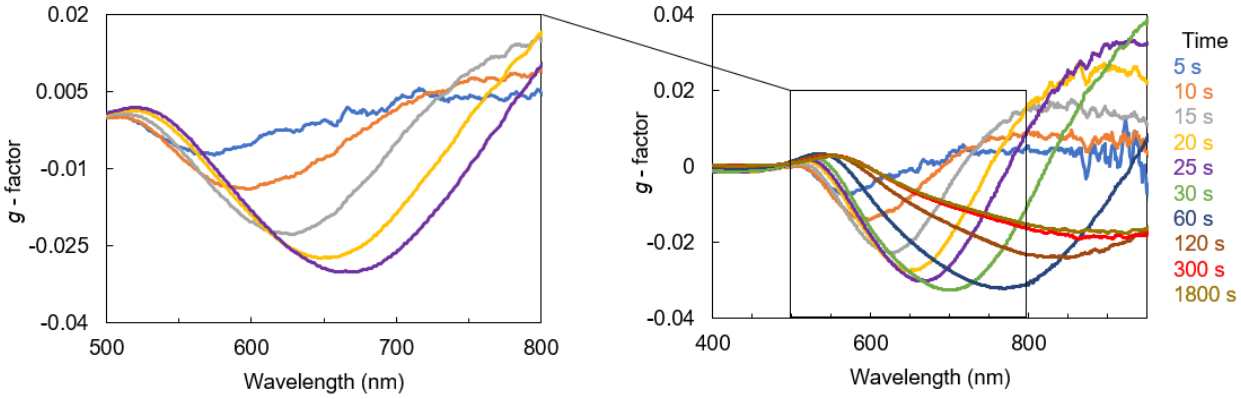

Figure S7. Chiroptical factor spectra of nanoparticles isolated from a chiral growth reaction by $NaBH_4$ addition at different time intervals, using penta-twinned Au NR seeds and *R*-BINAMINE as the chiral inducer.

Figure S8. Additional electron tomography reconstructions for the kinetic series shown in **Figure 4** of the main text. Nanoparticles were isolated from a chiral growth reaction with penta-twinned Au NR seeds and *S*-BINAMINE by $NaBH_4$ addition after 10 and 15 s. The scale bar is 25 nm.

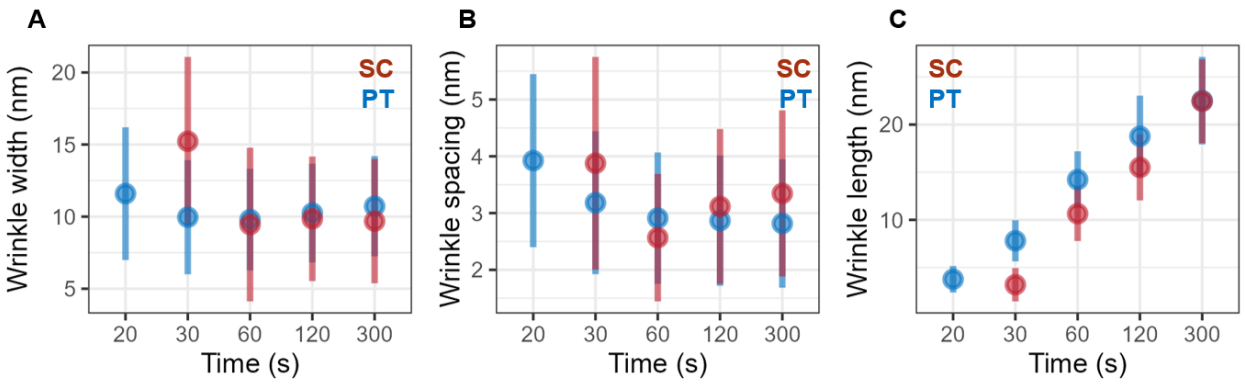

Figure S9. Measurements of (A) wrinkle width, (B) interwrinkle spacing and (C) wrinkle length over time, from the timepoint of clear wrinkle definition at the surface of the particles (30 s in the series grown on single-crystalline seeds, 20 s in the series grown on penta-twinned seeds).

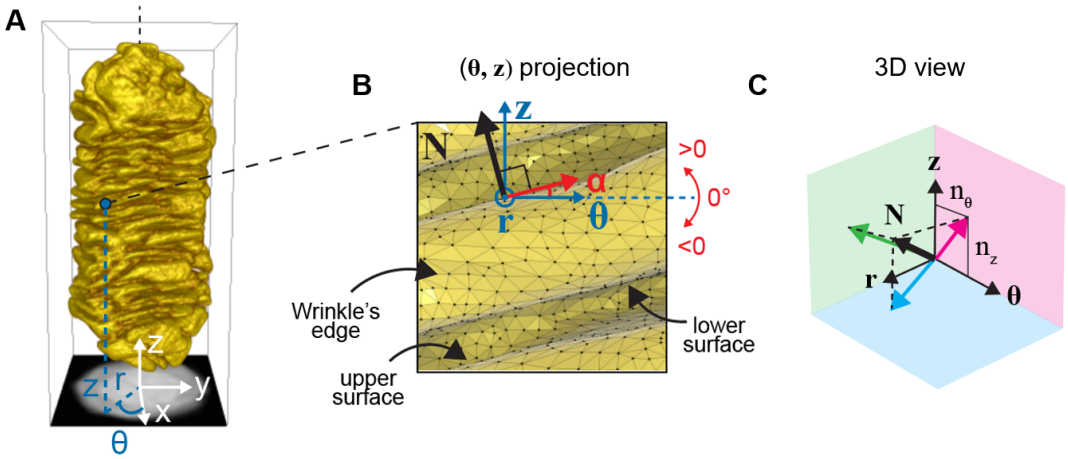

Figure S10. Definition and illustration of the helical inclination angle α. The normal vector **N** of each surface element of the triangulated mesh (A) of a NR can be expressed in a local cylindrical basis (B, C). In this basis, the (**θ, z**) component (magenta in C) of **N** is related to α by equation 2 (**Methods**). α will be positive for a right-handed feature as depicted in (B), negative for a left-handed feature. As detailed in the **Supplementary discussion**, the wrinkle's edge is effectively non-inclined because it will typically have as many elements inclined positively as negatively due to the way α is calculated; it is the lower and upper surfaces of the wrinkles that will contribute to an excess of right- or left-handed surface area.

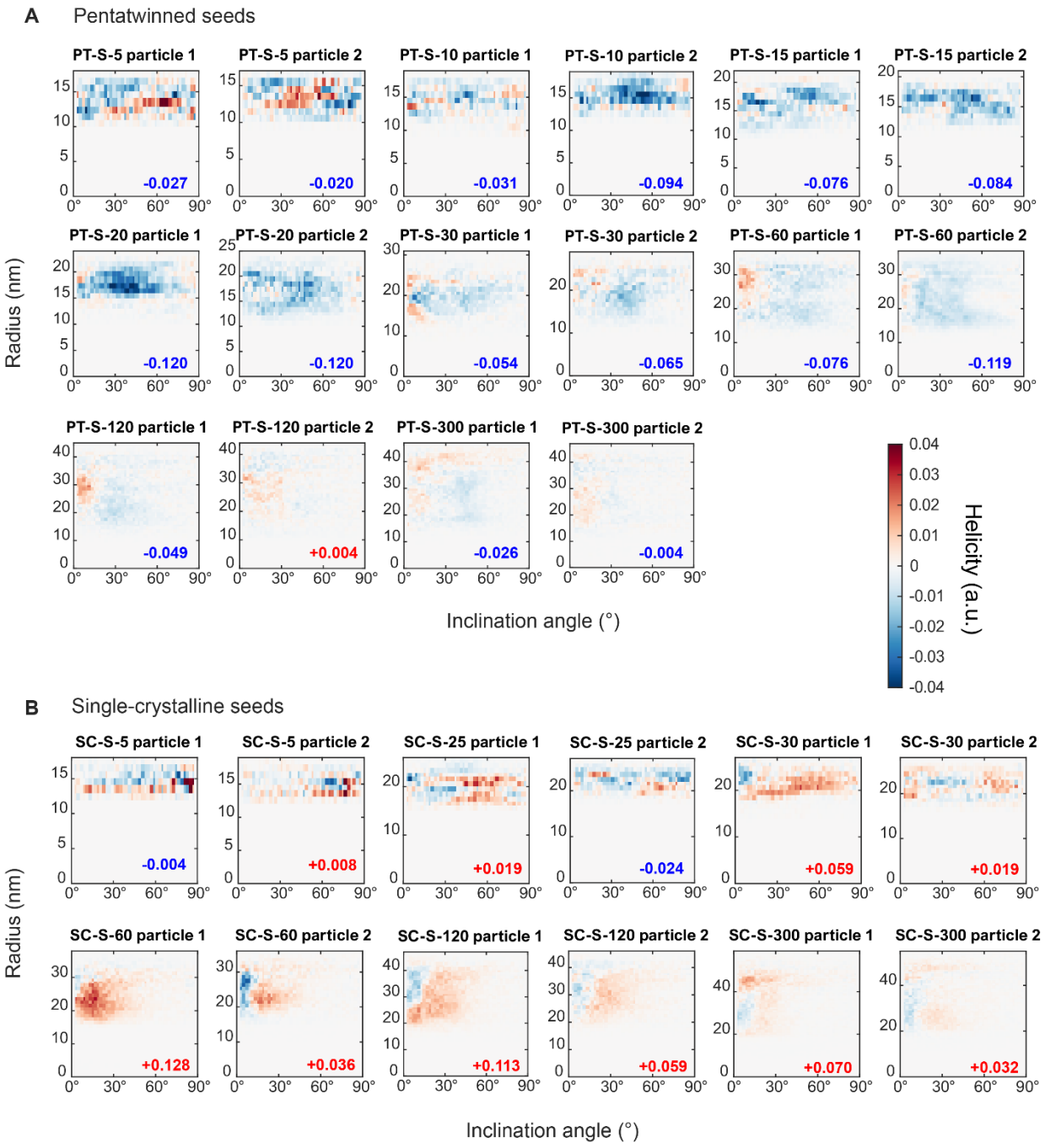

Figure S11. Helicity plots of all particles analyzed in the kinetic series of the chiral growth reactions on PT and SC seeds with *S*-BINAMINE. The total helicity is indicated in the lower right corner of each plot and is color coded following the helicity color bar. Red, positive helicity indicates right-handedness, blue, negative helicity, indicates left-handedness.

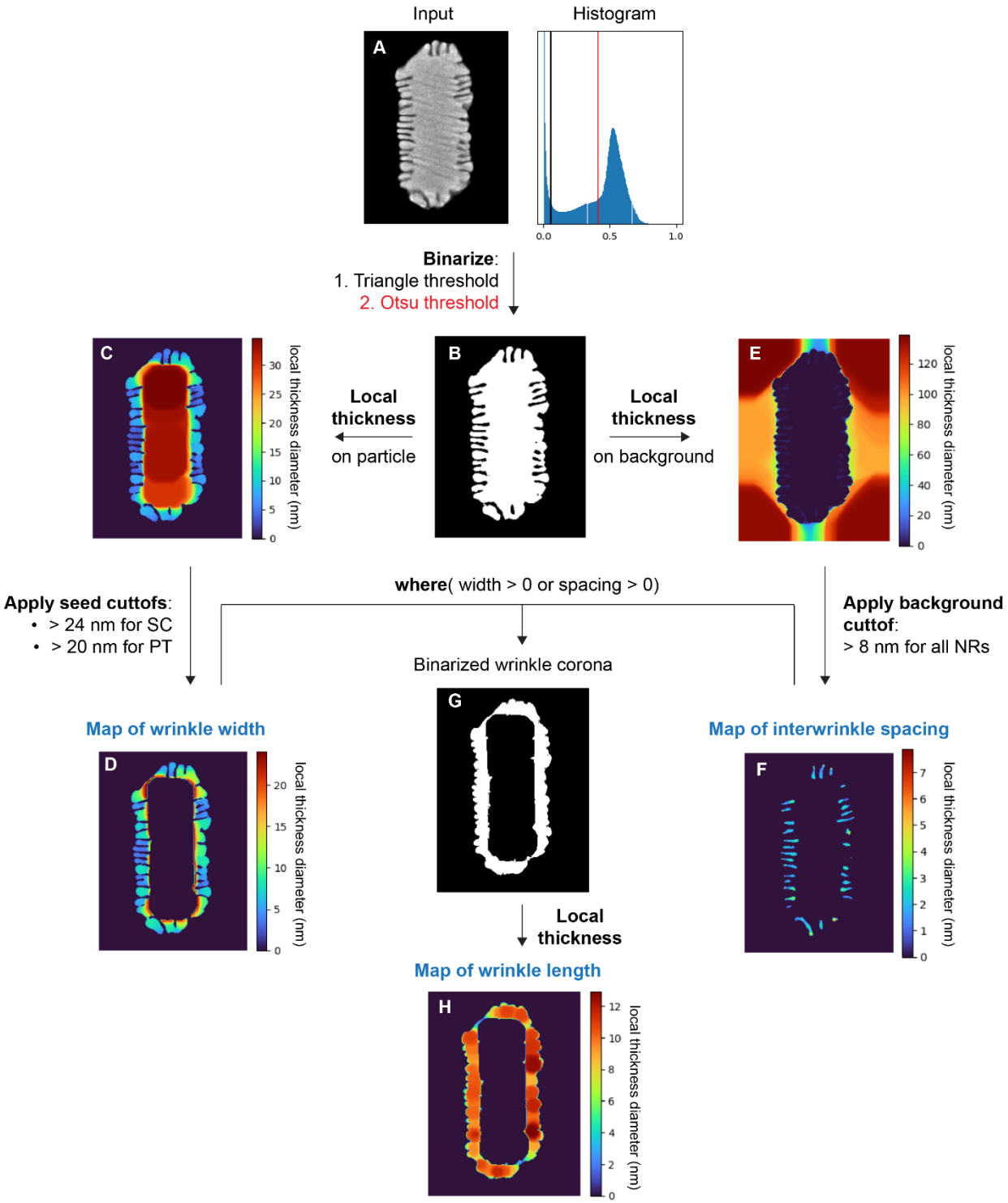

Figure S12. Workflow for automated wrinkle width, length, and interspacing extraction from electron tomography reconstructions. A central orthoslice is shown at each step but all operations were performed in 3D.

Supplementary Table S1

Table S1. Summary statistics of wrinkle morphological measurements

Seed	Time	Thickness (nm)		Interwrinkle spacing (nm)		Length (nm)	
		mean	std	mean	std	mean	std
PT	20	11.60	4.60	3.93	1.52	3.86	1.49
PT	30	9.97	3.96	3.19	1.26	7.94	2.36
PT	60	9.79	3.52	2.91	1.16	14.31	3.05
PT	120	10.23	3.42	2.86	1.15	18.79	4.28
PT	300	10.73	3.48	2.82	1.13	22.55	4.59
SC	30	15.21	5.85	3.87	1.87	3.15	1.73
SC	60	9.43	5.33	2.56	1.12	10.51	2.95
SC	120	9.84	4.32	3.11	1.36	15.49	3.47
SC	300	9.68	4.31	3.34	1.46	22.09	4.73

Supplementary References

1. González-Rubio, G.; Kumar, V.; Llombart, P.; Díaz-Nunez, P.; Bladt, E.; Altantzis, T.; Bals, S.; Peña-Rodríguez, O.; Noya, E. G.; MacDowell, L. G.; Guerrero-Martínez, A.; Liz-Marzán, L. M., Disconnecting Symmetry Breaking from Seeded Growth for the Reproducible Synthesis of High Quality Gold Nanorods. *ACS Nano* **2019**, *13*, 4424-4435.
2. González-Rubio, G.; Llombart, P.; Zhou, J.; Geiss, H.; Peña-Rodríguez, O.; Gai, H.; Ni, B.; Rosenberg, R.; Cölfen, H., Revisiting the Role of Seed Size for the Synthesis of Highly Uniform Sub-10 nm Length Gold Nanorods. *Chem. Mater.* **2024**, *36*, 1982-1997.
3. Sánchez-Iglesias, A.; Jenkinson, K.; Bals, S.; Liz-Marzán, L. M., Kinetic Regulation of the Synthesis of Pentatwinned Gold Nanorods below Room Temperature. *J. Phys. Chem. C* **2021**, *125*, 23937-23944.
4. Sánchez-Iglesias, A.; Winckelmans, N.; Altantzis, T.; Bals, S.; Grzelczak, M.; Liz-Marzán, L. M., High-Yield Seeded Growth of Monodisperse Pentatwinned Gold Nanoparticles through Thermally Induced Seed Twinning. *J. Am. Chem. Soc.* **2017**, *139*, 107-110.
5. González-Rubio, G.; Mosquera, J.; Kumar, V.; Pedrazo-Tardajos, A.; Llombart, P.; Solís, D. M.; Lobato, I.; Noya, E. G.; Guerrero-Martínez, A.; Taboada, J. M.; Obelleiro, F.; MacDowell, L. G.; Bals, S.; Liz-Marzán, L. M., Micelle-Directed Chiral Seeded Growth on Anisotropic Gold Nanocrystals. *Science* **2020**, *368*, 1472-1477.
6. Heyvaert, W.; Pedrazo-Tardajos, A.; Kadu, A.; Claes, N.; González-Rubio, G.; Liz-Marzán, L. M.; Albrecht, W.; Bals, S., Quantification of the Helical Morphology of Chiral Gold Nanorods. *ACS Materials Lett.* **2022**, *4*, 642-649.
7. Zhuo, X.; Mychinko, M.; Heyvaert, W.; Larios, D.; Obelleiro-Liz, M.; Taboada, J. M.; Bals, S.; Liz-Marzán, L. M., Morphological and Optical Transitions during Micelle-Seeded Chiral Growth on Gold Nanorods. *ACS Nano* **2022**, *16*, 19281-19292.
8. Spaeth, P.; Adhikari, S.; Heyvaert, W.; Zhuo, X.; García, I.; Liz-Marzán, L. M.; Bals, S.; Orrit, M.; Albrecht, W., Photothermal Circular Dichroism Measurements of Single Chiral Gold

Nanoparticles Correlated with Electron Tomography. *ACS Photonics* **2022**, *9*, 3995-4004.
9. Vanrompay, H.; Skorikov, A.; Bladt, E.; Béché, A.; Freitag, B.; Verbeeck, J.; Bals, S., Fast versus Conventional HAADF-STEM Tomography of Nanoparticles: Advantages and Challenges. *Ultramicroscopy* **2021**, *221*, 113191.
10.van Aarle, W.; Palenstijn, W. J.; De Beenhouwer, J.; Altantzis, T.; Bals, S.; Batenburg, K. J.; Sijbers, J., The ASTRA Toolbox: A Platform for Advanced Algorithm Development in Electron Tomography. *Ultramicroscopy* **2015**, *157*, 35-47.
11. van Aarle, W.; Palenstijn, W. J.; Cant, J.; Janssens, E.; Bleichrodt, F.; Dabravolski, A.; De Beenhouwer, J.; Joost Batenburg, K.; Sijbers, J., Fast and Flexible X-Ray Tomography Using the ASTRA Toolbox. *Opt. Express* **2016**, *24*, 25129-25147.
12. Sa, J.; Hu, N.; Heyvaert, W.; Van Gordon, K.; Li, H.; Wang, L.; Bals, S.; Liz-Marzán, L. M.; Ni, W., Spontaneous Chirality Evolved at the Au–Ag Interface in Plasmonic Nanorods. *Chem. Mater.* **2023**, *35*, 6782-6789.
13. Van Gordon, K.; Ni, B.; Girod, R.; Mychinko, M.; Bevilacqua, F.; Bals, S.; Liz-Marzán, L. M., Single Crystal and Pentatwinned Gold Nanorods Result in Chiral Nanocrystals with Reverse Handedness. *Angew. Chem. Int. Ed.* **2024**, *63*, e202403116.
14. Zack, G. W.; Rogers, W. E.; Latt, S. A., Automatic Measurement of Sister Chromatid Exchange Frequency. *J. Histochem. Cytochem.* **1977**, 25, 741–753.
15. Otsu, N. A., Threshold Selection Method from Gray-Level Histograms. *IEEE Trans. Syst., Man, Cybernetics*. **1979**, 9, 62–66.
16. Dahl, V. A.; Dahl, A. B., Fast Local Thickness. in *Proceedings of the IEEE/CVF Conference on Computer Vision and Pattern Recognition*. **2023**, 4335-4343.